



Visible light enhanced thermocatalytic CO + NO reaction over metastable NiCo₂O₄ catalyst

Gang Cheng ^{a,c}, Zehua Cai ^{a,b}, Xinjie Song ^{a,b}, Xun Chen ^{a,b}, Wenxin Dai ^{a,b,*}, Xianzhi Fu ^{a,**}

^a Research Institute of Photocatalysis, State Key Laboratory of Photocatalysis on Energy and Environment, Fuzhou University, Fuzhou 350108, China

^b Qingyuan Innovation Laboratory, Quanzhou 362801, China

^c Institute of Energy Research, Jiangxi Academy of Science, Nanchang 330096, China



ARTICLE INFO

Keywords:
NO reduction
Carbon monoxide
NiCo₂O₄
VOs
Photo-thermal effect

ABSTRACT

A NiCo₂O₄ catalyst was evaluated for CO + NO reaction under a photo-thermal synergistic effect. Compared with crystalline samples, metastable NiCo₂O₄ with a crystalline/amorphous heterostructure exhibited higher catalytic activity due to its better low temperature reducibility and more oxygen vacancies (VOs). The collective TPR, XPS, and *in-situ* DRIFTS results revealed that more VOs induced by CO directly interacting with the lattice oxygen of NiCo₂O₄ could promote NO adsorption and activation, and visible light irradiation further reinforced the above processes by facilitating CO to capture lattice oxygen and enriching electrons in VOs. With the increase in reaction temperature, the electron-rich VO_s could further drive NO dissociation into N₂. Herein, the VO_s was not only an active center of catalytic reaction, but also acted as a bridge between CO and NO for lattice oxygen circulation. Thus, a photo-thermal synergistic effect for NO reduction by CO occurred over metastable NiCo₂O₄.

1. Introduction

Nitric oxide (NO) mainly emitted from the combustion of various stationary sources and automobile engines caused many hazardous problems to the environment and human health [1,2]. The catalytic reduction of NO_x by CO as one of the most promising methods for denitrification has been extensively studied [2,3]. In the past few years, supported Platinum-group metals (PGMs, such as Rh, Pd, Pt) based catalysts exhibited remarkable catalytic performances for CO + NO reaction [2,4,5]. Our previous works also confirmed that introducing light into the thermo-catalytic CO + NO reaction over Pt/CeO₂-TiO₂, Pd/LaFeO₃, and Pd/N-TiO₂ could promote the adsorption of CO or NO and their activation on respective catalyst surface due to the enrichment in surface electron density of noble metals nanoparticles, and then obtained a high NO reduction efficiency [6–8]. Whereas, the high cost, limited availability, and high sintering rate at high temperature of PGMs hindered their large-scale applications. With regard to NO reduction by CO, the adsorption and dissociation of NO were deemed as the key steps, while oxygen vacancies (VOs) could effectively activate N-O bond to facilitate its dissociation [2,5,9–11]. Therefore, many efforts have been also spent on developing PGMs-free based catalysts for NO_x reduction,

especially the mixed oxide or supported transition metal compounds, by tuning their VO_s concentration [9,12–15].

Among them, cobalt-based catalysts had been widely applied for NO purification due to their excellent capacity for NO adsorption and activation. For example, Wang et. al reported that Co species in Fe-Co/ASC catalyst acted as active sites to transform NO into nitrates oxides for CO + NO reaction [10]. Roy et. al and Peck et. al respectively elaborated that spine Co₃O₄ exhibited a positive effect on NO decomposed into N₂O, and the excellent performance over which could be attributed to: I) the easy removal of lattice oxygen at low temperature due to the weak Co-O bond; II) the co-existence of redox Co³⁺/Co²⁺ during the NO decomposition process [16,17]. But even so, cobalt species could only catalyze the NO to N₂O normally at low temperature for CO + NO reaction (*i.e.* low N₂ selectivity) [18]. While the NO reduction over CuO-CoO binary oxides, Mn-modified Co₃O₄, and CoO_x-CeO₂ complex confirmed that the synergistic effect of multiple oxides derived from their strong interaction contributed to physicochemical properties of these catalysts, resulting in a better catalytic performance [3,15,19]. And for NO reduction, nickel or nickel oxide usually as a promoting additive was also widely applied in CO-SCR and NH₃-SCR processes [20, 21]. Another fact was that nickel could substitute cobalt at octahedral

* Corresponding author at: Research Institute of Photocatalysis, State Key Laboratory of Photocatalysis on Energy and Environment, Fuzhou University, Fuzhou 350108, China.

** Corresponding author.

E-mail addresses: daiwenxin@fzu.edu.cn (W. Dai), xzfu@fzu.edu.cn (X. Fu).

sites of Co_3O_4 to form a homogeneous solid solution due to their similar unit cell structures, and then affect the strength of metal-oxygen bond [22]. Wang et. al reported that bimetal NiCo_2O_4 with a better low-temperature reducibility, more surface adsorption oxygen species as well as synergistic effect between Ni and Co ions exhibited a higher H_2 -SCR performance than single Co_3O_4 or NiO [23]. The synergistic catalytic contribution of Co and Ni was also revealed in NH_3 -SCR process over $\text{MnO}_2@\text{NiCo}_2\text{O}_4$ catalyst [24]. Moreover, Duan et. al proposed that Ni substitution in Co-based spinel oxide would activate its lattice oxygen and then result in surface reconstruction of catalyst, which also provided the possibility for VOs formation [25]. More importantly, numerous studies indicated that both cobalt and nickel were favorite for the adsorption and activation of CO as well [26–29]. And that the synergic promoted effect between Ni and Co was also observed in CO oxidation at low temperature due to enhanced NiO dispersion and increased surface oxygen vacancies in catalyst [30]. Based on these, we considered that the ternary oxide NiCo_2O_4 could be regarded as a promising candidate for $\text{CO} + \text{NO}$ reaction at low temperature.

Moreover, NiCo_2O_4 as a P-type semiconductor with a narrow band gap has been also applied in photocatalytic CO_2 reduction, degradation of methylene blue and as photocathodes for PEC water splitting due to its multiple redox states, fast charge transfer rate and abundant VOs [31–34]. Specially, the tetrahedral high spin Co^{2+} ($\text{eg}^4\text{t}_{2g}^3$), octahedral low spin Co^{3+} (t_{2g}^6), and Ni^{3+} ($\text{t}_{2g}^6\text{e}_g^1$) constituted its electron configuration, in which O2p orbital served as valence band while metal (Ni, Co) 3d orbital as conduction band [35]. According to some reports and our previous works, the light irradiating catalysts could promote or induce VOs generation and stabilization, and then resulted in an improvement in catalytic performance [36–39], which further inspired us to execute $\text{CO} + \text{NO}$ reaction over the reducible NiCo_2O_4 under visible light illumination. And also, numerous researches affirmed that incorporating amorphous phase into catalysts could obviously improve the catalytic performances by increasing more coordination unsaturated sites and surface defects. For example, Kuang et. al reported that amorphous/crystalline hetero-phased Co-Fe-V hydroxide nanosheet exhibited an excellent catalytic performance toward OER compared to its crystalline and amorphous counterparts due to exposing more active sites [40]. Similarly, Li et. al also demonstrated that amorphous CoFe oxide with rich oxygen vacancies growing on 2D black phosphors could be transformed into different active sites under different reducing and oxidizing environments, simultaneously resulting in the enhancement of HER and OER performance [41]. And the similar results was also revealed in containing Ni specie catalysts [42]. In terms of NO removal, a stronger cooperative effect of different metals observed in amorphous mesoporous MnCeSmTiO_x mixed oxide also contributed to the desired SO_2 -tolerant and NH_3 -SCR capability at low temperatures [43]. And that SnO_2 with a crystalline/amorphous stacking structure was more favorite for regulating the adsorption of reactive molecules, promoting electron transfer and ROS formation, finally achieved an excellent NO oxidation activity [44].

Taking into account these aspects mentioned above, in this work, we separately prepared metastable and crystalline NiCo_2O_4 samples by a two-step solvothermal-calcination method, and then studied the photo-thermal synergistic effect on $\text{CO} + \text{NO}$ reaction over them at low temperature. Compared with crystalline NiCo_2O_4 , metastable sample with a crystalline/amorphous heterostructure exhibited better catalytic activity and higher N_2 selectivity. And the excellent catalytic performance of metastable NiCo_2O_4 could be attributed to the much stronger mobility of its surface lattice oxygen and more VOs in it, which was in favor of adsorption and dissociation of NO. Visible light irradiation further accelerated the VOs formation by enhancing the ability of CO capturing surface oxygen lattice of catalyst, while VOs with enriched electrons boosted NO adsorption and activation. After a series of characterizations and discussions, a possible mechanism for the photo-thermal synergistic promoted NO reduction by CO over metastable NiCo_2O_4 was proposed.

2. Experimental sections

2.1. Catalyst preparation

The NiCo_2O_4 precursor was prepared by a facile solvothermal method. Firstly, 1.5 mmol of $\text{Ni}(\text{NO}_3)_2 \cdot 6\text{H}_2\text{O}$, 3 mmol of $\text{Co}(\text{NO}_3)_2 \cdot 6\text{H}_2\text{O}$, and 15 mmol of urea were added into 60 mL mixture solution (20 mL distilled water and 40 mL ethylene glycol) in order under stirring at room temperature. After stirring for 1 h, the obtained transparent solution was transferred into a 100 mL Teflon-lined autoclave and then heated at 110 °C for 16 h in an electric oven. After cooling down to room temperature, the produced solid precipitate was separated from the residual solution by centrifugation and washed alternately with distilled water and ethanol several times, and then dried at 80 °C for 48 h. Based on the TG-DSC data (Fig. S1, ESI), the prepared precursor powder (XRD pattern in Fig. S2) was finally ground and then calcined at 250, 450, and 650 °C in static air for 3 h at a ramping rate of 1 °C min⁻¹ to harvest the NiCo_2O_4 products, named as NCO-250, NCO-450, and NCO-650, respectively. For the clarity of discussion, the NiCo_2O_4 samples in this work used for characterizations and photocatalytic reactions are the NCO-250 unless otherwise stated.

2.2. Characterization of catalysts

Simultaneous thermogravimetric (TG) and differential scanning calorimetry (DSC) analysis were conducted on a Netzsch STA 449 F3 thermoanalyzer with a heating rate of 10 °C min⁻¹ from 30 to 800 °C under an air of 50 mL min⁻¹. The X-ray diffraction patterns (XRD) patterns were recorded on a Bruker D8 advance powder X-ray diffractometer using Cu K α irradiation ($\lambda = 0.15418$ nm) operated at 40 kV and 40 mA. The mean crystallite size was determined by the strongest peak of the sample with the Debye-Scherrer-equation $d = K\lambda/b\cos\theta$. Fourier transform infrared spectra (FTIR) were performed on a Thermo Fisher Scientific iS50 FT-IR instrument, where the KBr powders was mixed with the samples and then pressed into appropriate disks. Raman spectra were collected on Renishaw invia Confocal microscopic Raman microscope employing a 532 nm excitation of Ar⁺ ion laser. The Brunauer-Emmett-Teller (BET) specific surface area and the pore size distribution curves of samples were determined using a Micromeritics ASAP 2020 surface area analyser with nitrogen adsorption at 77 K. The morphologies and structures of catalysts were taken on a Hitachi SU8010 field emission scanning electron microscope (SEM) and transmission electron microscopy (TEM, JEOL JEM-2010EX with field emission gun at 200 kV). The compositions of the samples were analyzed by energy-dispersive X-ray spectroscope (EDX) attached to the TEM instrument. The DRS was recorded at room temperature by a UV-vis spectrophotometer (Agilent, Cary 500) equipped with an integrating sphere and BaSO₄ was employed as a reference. The XPS measurements were performed on a Thermo Fisher Scientific ESCALAB 250Xi spectrometer system by using the Al-K α X-ray beam (1486.6 eV) with the C1s (284.8 eV) as a reference. Electron paramagnetic resonance (EPR) signals of the samples were recorded using a Bruker A300 spectrometer under vacuum at 77 K. For quasi *in situ* EPR testing, the samples were firstly pretreated by vacuum heating treatment at 200 °C for 1 h to eliminate the other impurities. After cooling down to 150 °C, the reactions were performed under different feed streams or not, and the visible light irradiated the sample at the identical conditions by a 100 W high-pressure mercury lamp.

Temperature programmed reduction measurements of catalyst samples by H_2 (H₂-TPR) were carried out at a Micromeritics ASAP 2920 instrument equipped with a thermoconductivity detector (TCD). Prior to the introduction of H_2 , the powder samples (100 mg) were pretreated in a high-purity He stream (50 mL min⁻¹) at 300 °C for 60 min. After cooling to 50 °C in Helium stream, H₂-TPR experiments were executed in the temperature range 50–300 °C at a ramping rate of 10 °C min⁻¹ in 5.0 vol% H_2/Ar stream (50 mL min⁻¹) accompanied with the recording

of a TCD signal. The CO-TPR was executed under a similar condition except that the purge gas was 5.0 vol% CO/Ar instead of 5.0 vol% H₂/Ar, and then the CO-TPR was conducted from room temperature to 250 °C at a heating rate of 5 °C min⁻¹. CO, CO₂, and H₂O in the outlet gas were recorded by a OmniStar mass spectrometer equipped with the software Quadstar 32-bit.

2.3. Catalytic activity evaluation

The catalytic performances of prepared catalyst samples for NO reduction by CO were conducted in a self-designed flow fixed-bed micro-reactor under an atmospheric pressure. The schematic illustration of the reactor was profiled in Fig. S3. In the typical reaction, the 160 mg catalyst with a grain size of 0.2–0.3 mm was packed in a flat-plate square quartz cell (20 × 20 × 0.5 mm, ensuring the interaction of light and the majority sample) with a circulating silicone oil system which could make the samples heated to 220 °C. The actual temperature of the catalyst bed was monitored by a K-type thermocouple inserted into the reactor. During the photo-thermal reaction process, catalyst samples were irradiated from the top surface of the quartz cell by a 300 W PLS-SXE300D xenon lamp with a visible light filter (420 nm < λ < 760 nm, Beijing Perfectlight Co., Ltd.). As testing the pure thermal reaction without light, the quartz cell was enclosed by an Al foil to rule out light irradiation. The feed stream composed of 1500 ppm NO, 1500 ppm CO, 5% H₂O (when used), and the balance gas N₂ was fed at a total flow rate of 100 mL min⁻¹, and the corresponding gaseous hourly space velocity (GHSV) was 30,000 h⁻¹. Before introducing the reaction gas stream into the reaction system, the catalyst samples were first pretreated in high-purity N₂ atmosphere at 150 °C for 2 h with the flow rate 70.0 mL min⁻¹. After cooling down to room temperature, the reactions were performed under feed streams at a series of temperatures with an interval of 20 °C from 60 to 220 °C. After reacting for 1 h at each temperature in the dark, visible light was introduced into the reactor for another 1 h. The effluent gases were analyzed by an online connected Photoacoustic spectrum analyzer (CO, CO₂, N₂O, NO₂, and H₂O, GASERA ONE, Beijing DuKe) and NO_x analyzer (NO, Testo 340). The NO conversion, CO conversion, and N₂ selectivity were calculated as follow, respectively:

$$\text{NO conversion (\%)} = \frac{[\text{NO}]_{\text{in}} - [\text{NO}]_{\text{out}}}{[\text{NO}]_{\text{in}}} \times 100\%$$

$$\text{CO conversion (\%)} = \frac{[\text{CO}]_{\text{in}} - [\text{CO}]_{\text{out}}}{[\text{CO}]_{\text{in}}} \times 100\%$$

$$\text{N}_2 \text{ selectivity (\%)} = (1 - \frac{2[\text{N}_2\text{O}]_{\text{out}}}{[\text{NO}]_{\text{in}} - [\text{NO}]_{\text{out}}}) \times 100\%$$

2.4. Chemisorptions of NO and CO

In situ DRIFTS were collected on a Bruker V880 instrument equipped with a high-sensitivity MCT detector (cooled by liquid N₂ at 77 K). The spectra were recorded from 1000 to 4000 cm⁻¹ at a spectral resolution of 4 cm⁻¹ (the times of scans at 64). The DRIFTS cell (Harrick) was fitted with two BaF₂ windows and a heating cartridge, which could heat catalyst samples to 600 °C. Prior to each experiment, the sample was pretreated in high-purity N₂ stream (50 mL min⁻¹) at 300 °C for 1 h to eliminate the other impurities. The backgrounds of samples were collected after cooling down to ambient temperature. And then the samples were exposed to a controlled stream of 1500 ppm CO or 1500 ppm NO in He for 30 min to be saturated, followed by heating at a simulated reaction condition. Then all of the spectra were obtained by subtraction of the corresponding background references. For comparison, the visible light irradiated the sample at the identical temperature by a 100 W high-pressure mercury lamp through a quartz window located on the dome of DRIFTS cell.

3. Results and discussion

3.1. Structure and morphology properties

Firstly, the morphology of synthesized sample was characterized by SEM. As shown in Fig. S4, there was a significant microstructure evolution observed from a stack of randomly oriented nanorods in NCO-250 to irregular nanoparticles in NCO-450 and NCO-650. In detail, note that the metastable NCO-250 exhibited more pore structure and rougher surface compared to other two samples, which could be owing to its incomplete crystallinity at a relatively low calcination temperature. This result was supported by the textural property analyses of these catalysts as well. As presented in Fig. S5 and Table S1, the larger specific surface area and BJH pore volume in NCO-250 provided more possibility for reactants diffusion and activation for long-term NO and CO removal.

TEM images of NCO-250 sample displayed in Fig. 1a and b further revealed its microscopic nanorod structure with a diameter of about 30 nm. Also, well-defined diffraction rings observed in the selected-area electron diffraction (SAED) pattern (inset of Fig. 1b) revealed its polycrystalline characteristic, in line with subsequent XRD analysis. The high-resolution TEM (HRTEM) image of Fig. 1c exhibited that the NCO-250 was composed of the mixture of crystalline and amorphous phases (noted by red circles), which exactly verified aforementioned TG-DTA results. Therefore, the prepared NCO-250 samples in this work could be regarded as metastable NiCo₂O₄. The formation of amorphous phases could provide more defect sites, which could be favorite for NO adsorption and activation on catalyst. Moreover, the lattice spacings of 0.471, 0.285, 0.245, and 0.205 nm observed in Fig. 1c were indexed to the (111), (220), (311), and (400) plane of NiCo₂O₄ sample, respectively [23,45]. EDX analysis (Fig. S6) revealed high purities in NiCo₂O₄ sample with the Ni/Co atomic ratio to be 1:2, which was well coherent with primal chemical formula. The corresponding elemental mapping images in Fig. 1d exhibited a high uniform distribution of Ni, Co, and O elements across NiCo₂O₄ sample, which derived from a close proximity and strong interaction of these elements.

Further, the synthesized NiCo₂O₄ products were structurally characterized by powder XRD. As illustrated in Fig. 2a, the precursor calcined at 250, 450, and 650 °C all exhibited six well-defined diffraction peaks at 2θ of 18.8°, 31.2°, 36.8°, 44.5°, 59.0°, 65.1°, which exactly corresponded to (111), (220), (311), (400), (511), and (440) planes of typical cubic spinel structure (JCPDS No. 20-0781), respectively [33]. It was also observed that elevated calcination temperatures produced samples with higher crystallinity, also resulted in a noticeable increase in mean crystallite size calculated by Scherrer formula (Table S1). No other additional diffraction peaks were detected over NCO-250 and NCO-450 samples, indicating their high phase purity. Whereas four new diffraction peaks indexed to the (111), (200), (220), and (311) planes of NiO appeared in NCO-650 [23], which indicated the partial decomposition of NiCo₂O₄ phase during 650 °C heat treatment, consistent with the TG-DSC results (Fig. S1). However, compared with NCO-450 and NCO-650, the significantly broadened and negatively shifted XRD peaks (the inset of Fig. 2a) observed in NCO-250 sample suggested a disordered lattice volume, probably resulted from defect engineering [46,47]. The chemical structures of as-synthesized samples revealed by FTIR (Fig. S7) further suggested the formation of NiCo₂O₄ spinel phase, and weaker metal-oxygen bond in NCO-250 could enhance the mobility of lattice oxygen.

Typically, the Raman spectra also confirmed the structural information on the samples. As shown in Fig. 2b, all samples exhibited four similar bands at 184, 465, 501, and 652 cm⁻¹, corresponding to F_{2g}, E_g, F_{2g}, and A_{1g} four Raman vibration modes of spine structured NiCo₂O₄, respectively [48]. Moreover, the peaks at 327 cm⁻¹ could be also related to the vibration mode of NiCo₂O₄ with spine phase [49], while 1045 cm⁻¹ attributed to the 2LO mode of Ni-O vibration [50]. And similar to XRD results, the weaker Raman peaks of NCO-250 than that of NCO-450 and NCO-650 implied its poorer crystallinity and decreased

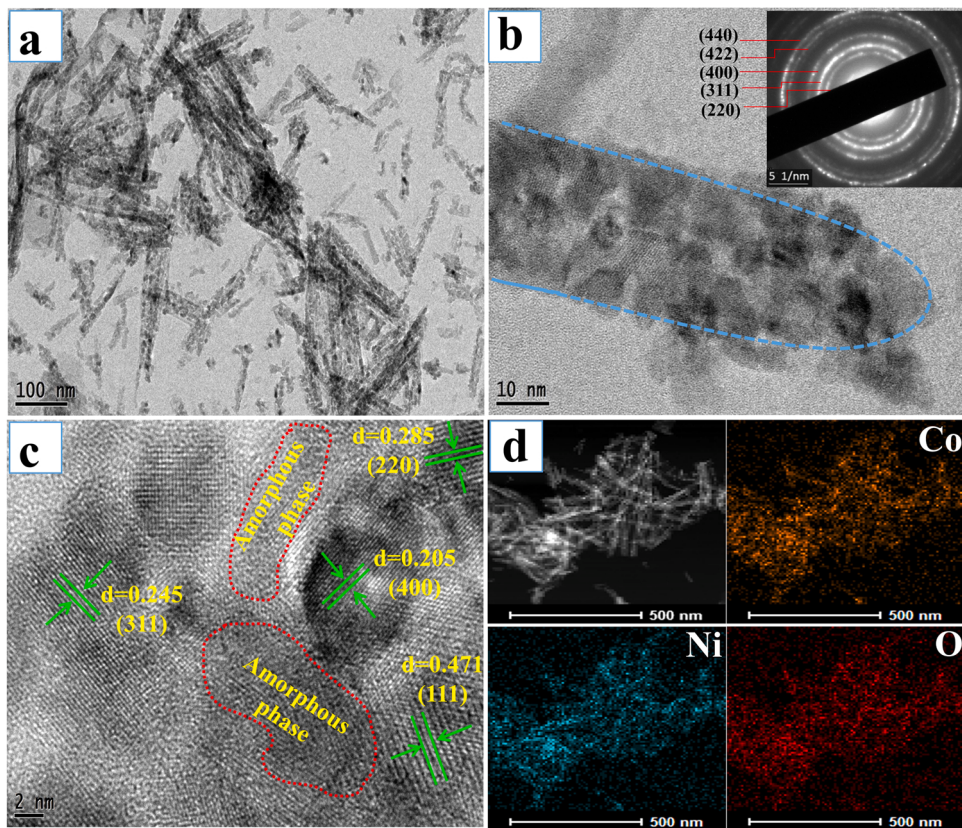


Fig. 1. (a, b) TEM images, (c) HRTEM image, (d) HADDF-STEM image and corresponding elemental mapping results of NiCo_2O_4 sample.

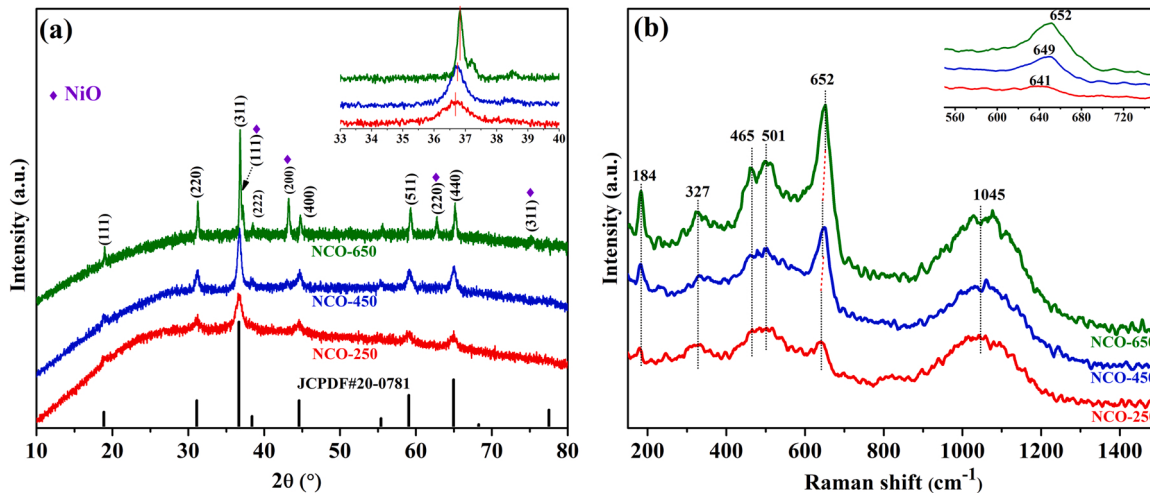


Fig. 2. (a) XRD patterns and (b) Raman spectra of NCO-250, NCO-450, and NCO-650 samples.

crystalline size [38,51]. Compared with NCO-450 and NCO-650 samples, the obvious negatively shifted A_{1g} bands (ca. at 650 cm^{-1} , inset of Fig. 2b) in NCO-250 also suggested that NCO-250 possessed more highly defective structure induced by oxygen vacancies [48,52,53], which was more beneficial to adsorb and activate CO and NO.

According to the previous reports [45,47,53], the XPS results could give more detailed information on chemical bonds of the samples and VOs. Thus, we used it to analyze the VOs content in the three samples. As shown in Fig. 3a for the O1s core-level XPS spectra, three peaks observed at ca. 529.5 eV (O_1), 531.1 eV (O_2), and 532.5 eV (O_3) could be ascribed to lattice oxygen bonded to metal, oxygen species adjacent to the defects or VOs with low coordination, and hydroxyl species mainly stemmed

from adsorbed water molecules, respectively [45,47]. Notably, the area ratio of O_2 peak to the sum of ($\text{O}_1 + \text{O}_2 + \text{O}_3$) peaks was gradually decreased from the NCO-250 to NCO-650, revealing that the relative amount of VOs followed the order: NCO-250 > NCO-450 > NCO-650. The results also indicated that metastable NCO-250 sample calcined at a lower temperature possessed a stronger lattice oxygen mobility, which usually led to a higher catalytic activity. Meanwhile, the presence of mixed valence cobalt and nickel also provided the possibility of VOs formation and lattice oxygen circulation (Fig. S8). Additionally, the obviously positive BE values of Co_{2p} and Ni_{2p} in NCO-250 compared to another two samples could be related to the co-existence of amorphous phase in its crystallization structure [54], further indicating its

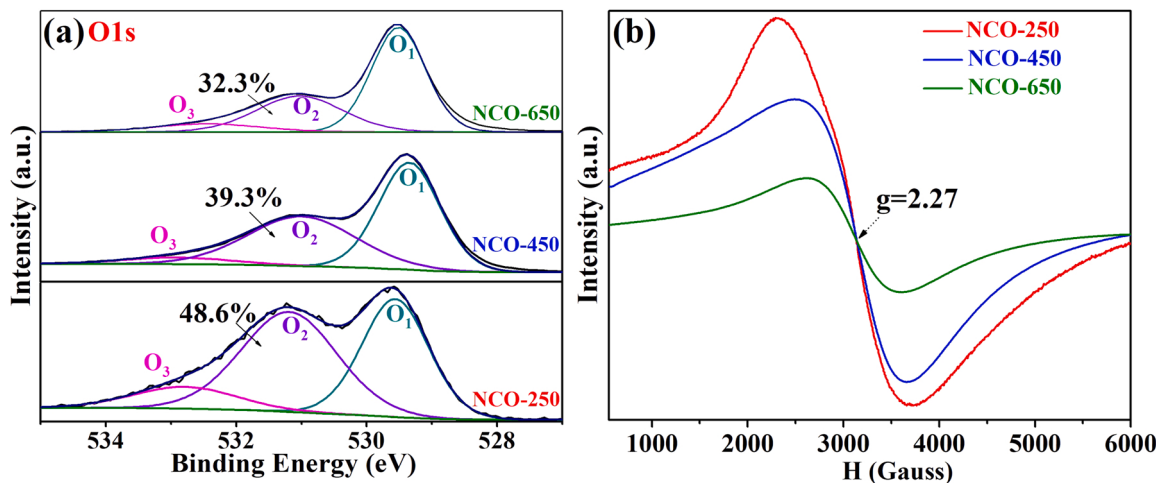


Fig. 3. (a) XPS spectra for the O1s level and (b) Room temperature ESR spectra of NCO-250, NCO-450, and NCO-650 samples.

metastable characteristics.

Additionally, EPR analysis was further executed to get more direct evidence for defective structure of as-prepared samples. As displayed in Fig. 3b, a strong EPR signal at $g = 2.27$ ascribed to Co^{2+} (*i.e.* VOs) was detected in all NiCo_2O_4 samples [47,55]. However, the decreasing EPR peak with the increase in calcination temperature indicated that metastable NCO-250 possessed more VOs amount compared to other two samples, in line with above XRD, Raman, and XPS analyses. Therefore, based on the above joint characterizations and discussions, we could

safely conclude that the metastable NiCo_2O_4 sample with more VOs was successfully prepared by a facile two step solvothermal-lower temperature calcination.

3.2. Catalytic performances

For photocatalytic reaction, the defect feature of catalyst will greatly influence its charge carrier separation [38,53]. Given the superior ability of NiCo_2O_4 for absorbing visible light (Fig. S9), thus comparative

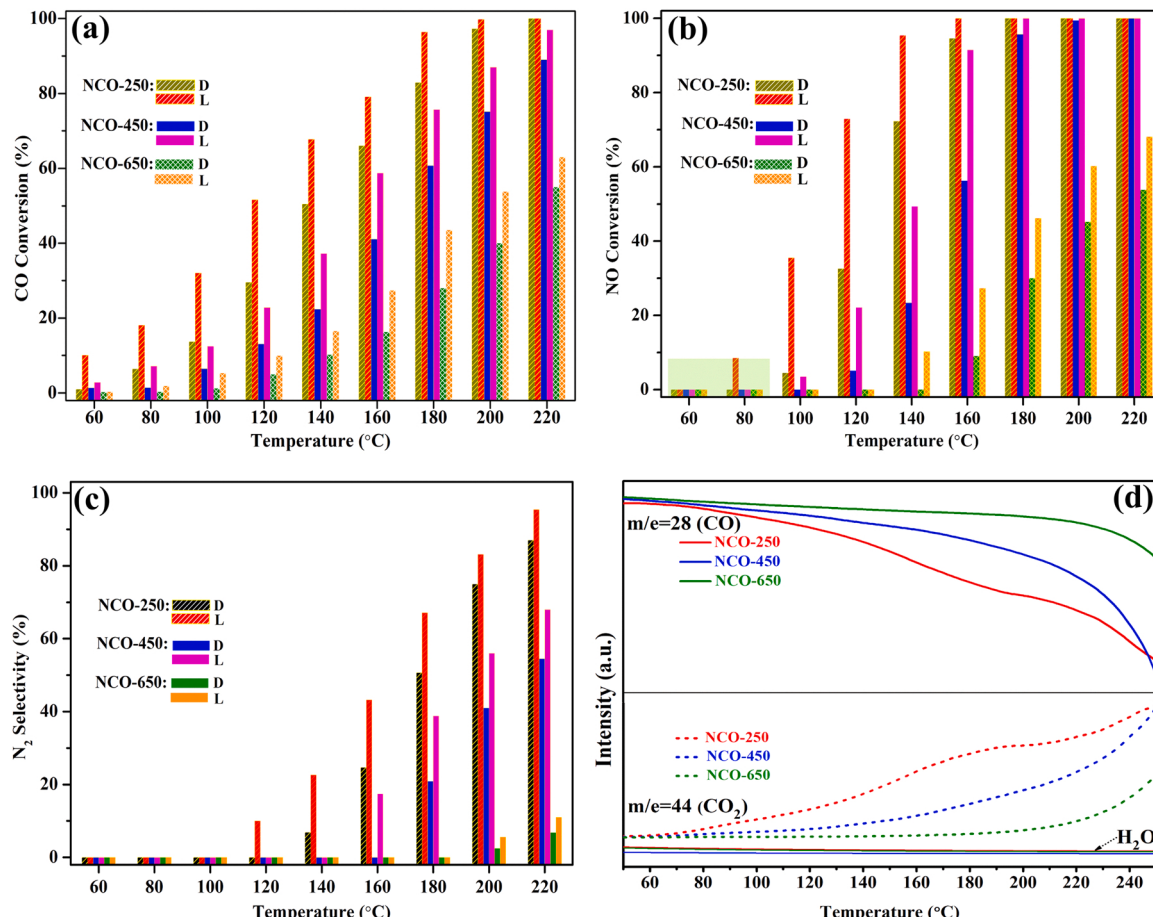


Fig. 4. (a) CO conversion, (b) NO conversion, and (c) N_2 selectivity at different reaction temperatures over different NiCo_2O_4 samples under visible light irradiation (L) or in dark (D). (d) CO-TPR-Mass profiles over different NiCo_2O_4 samples.

transient photocurrent characterization on the above three samples was systematically conducted. As evidenced in Fig. S10, a more obvious promotion of cathodic photocurrent response over VO_x-rich NCO-250 was observed relative to those over VO_x-poor counterparts, illustrating a more efficient carrier separation and charge transport. Moreover, the electron transfer behaviors of CO and NO over NiCo₂O₄ revealed by the gas sensing performances also confirmed the feasibility of promoting CO oxidation and NO reduction over under visible light irradiation (Fig. S11). Fig. 4 shows the corresponding catalytic performances of NiCo₂O₄ samples for CO + NO reaction under visible light irradiation or not. As can be seen in Fig. 4a, the CO conversion on all catalysts improved gradually with the increment of temperature from initial 60 °C, while visible light irradiation could further promote its conversion, especially at lower temperature. Note that the CO conversion over the NCO-250 was apparently higher than other two samples (following the order of NCO-250 > NCO-450 > NCO-650) and reached an 100% conversion only at 200 °C. The NO conversion over different NiCo₂O₄ samples exhibited a similar result as to that of CO (Fig. 4b). Herein, the NO conversion over NCO-250 sample was obviously initiated at 100 °C and then reached the maximum of 100% at 160 °C in light reaction, at which obviously superior to 91.0% and 27.0% conversion respectively over NCO-450 and NCO-650. The gradually reduced catalytic activities from NCO-250 to NCO-650 correctly corresponded to their sequentially reduced VO_x concentration and specific surface area due to increased bulk crystalline nature of the samples. Additionally, the negligible conversion of CO and NO (Fig. S12) below 200 °C over Ni-Co precursor could be attributed to a weak charge transfer in the photo-thermal redox reaction due to its quite poor crystallinity revealed in Fig. S2. Therefore, based on the above catalytic performances, we could further confirm that enriched defects in NiCo₂O₄ induced by metastable structure of amorphous/crystalline heterophase were more favorite for NO reduction by CO.

However, note that the NO presented a fairly low or negligible conversion below 100 °C (seeing the shadow in Fig. 4b) over all samples compared with CO, which indicated that CO at low temperature would directly react with surface lattice oxygen of catalyst sample instead of NO or surface hydroxyl to generate CO₂ via a Mars-van Krevelen mechanism. The speculation was well confirmed by both the CO₂ generation (Fig. S13a-c) and the negligible H₂O production revealed by CO-TPR results (Fig. 4d). The more vulnerable lattice oxygen over NCO-250 attacked by CO than that over NCO-450 and NCO-650 could result in more VO_x formation and then expedite NO dissociation. Therefore, the continuous improved temperature ($T \geq 100$ °C) would be favorite for the NO reduction by CO, while visible light irradiation further facilitated the process. For comparison, a controlled experiment (Fig. S13d) that NO reaction in the absence of CO over NiCo₂O₄ was also executed, while there was no any NO conversion observed in it. This result fully confirmed that NO could only be reduced by CO instead of autocatalytic decomposition.

More importantly, it could be found that N₂ selectivity over NCO-250 was also obviously superior to that over other two samples in dark, and visible light illumination further boosted N₂ production (Fig. 4c). Even so, note that N₂O was still the major reduced product at low temperature for NCO-250, which was mainly owing to a less dissociation energy of nitrate or nitrite to form N₂O and high activation energy of N₂O to N₂ [13], while elevating temperature would gradually convert N₂O to N₂. To sum up, the results of catalytic performances fully confirmed that metastable NiCo₂O₄ was both favorite for the NO reduction by CO and enhancing N₂ selectivity, and visible light irradiation would further accelerate this process. Nevertheless, the more detailed studies would be presented step by step in the following sections.

3.3. Reducible properties of catalysts (H₂-TPR) and stability testing of catalyst

To clarify the correlation between redox property and NO reduction

performance, the as-prepared samples were characterized by H₂-TPR. As illustrated in Fig. 5, there were two well-defined reduction peaks in NCO-450, which corresponded to stepwise reduction of NiCo₂O₄. The first peak at 234 °C was attributed to the reduction of NiCo₂O₄ to NiCoO₂ (i.e. Co³⁺ to Co²⁺ and Ni³⁺ to Ni²⁺), while the latter-a large overlapping peak with maximum at 342 °C could be assigned to a co-reduction of Co²⁺ to Co and Ni²⁺ to Ni [23,56]. Yet both the above reduction peaks over NCO-650 shifted to higher temperatures (288 °C and 371 °C), and a more apparent shoulder peak observed at 325 °C was attributed to the reduction of NiO (from the sample decomposition) to Ni [23]. Instead, the reduction peaks of NCO-250 shifted to lower temperatures 221 °C and 321 °C than those of NCO-450 and NCO-650, which further suggested a much stronger lattice oxygen mobility of metastable NCO-250 and then resulted in a much better low-temperature reducibility, also consistent with CO-TPR results. Note that a new reduction peak observed from ca. 70 °C onset temperature with maximum at 169 °C over NCO-250 was attributed to the reduction of surface chemisorbed oxygen, indicating its excellent oxygen storage capacity. Moreover, the much smaller reduction peak of Co³⁺ (Ni³⁺) to Co²⁺(Ni²⁺) in NCO-250 compared to other samples also confirmed the existence of more low-valence metal (i.e. VO_x) in it, corresponding well to the above-mentioned XPS and EPR results.

Based on the CO-TPR and H₂-TPR results, it was inferred that sample pre-treated by reductive CO gas could produce more VO_x, and then upgrade the NO dissociation and conversion. Therefore, a pretreatment for NiCo₂O₄ was conducted by a 1500 ppm CO at 150 °C, and the much poorer crystallinity revealed by corresponding XRD pattern (Fig. S14) indicated a more existence of amorphous state in it than that in fresh sample. Moreover, the O1s XPS spectra (Fig. 6a) and EPR analysis (Fig. 6b) of pre-reduced NiCo₂O₄ also confirmed more VO_x formed in it. The results suggested that the NiCo₂O₄ exposed into reductive CO stream at a certain temperature would cause a new surface reconstruction. Compared with fresh sample, the effectively boosted NO conversion (Fig. 6c) in dark reaction over pre-reduced NiCo₂O₄ at the identical condition as above well verified our hypothesis. However, the almost same NO conversion over two samples in light reaction also exactly confirmed the accelerated effect of visible light irradiating fresh NiCo₂O₄ on lattice removal and VO_x formation. Given this result, the catalytic stability of CO pre-reduced NiCo₂O₄ for CO + NO reaction was also investigated at 190 °C under visible light irradiation or in dark. As seen in Fig. 6d, the CO conversion over NiCo₂O₄ gradually decreased from 97.4% to 87.8% in dark with the prolonged reaction time, which could be due to the accumulation of large amounts of surface carbonate or nitrates species, and then block the active sites, while introducing visible light could further promote CO conversion and simultaneously retarded its attenuation. However, the NO conversion almost kept stable, especially under visible light irradiation. The decrease in CO

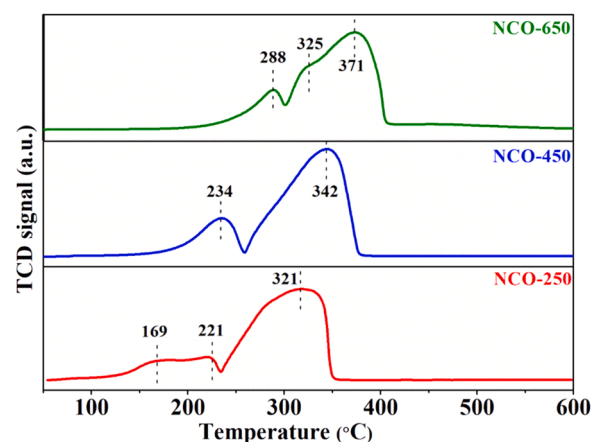


Fig. 5. H₂-TPR profiles of NCO-250, NCO-450, and NCO-650 samples.

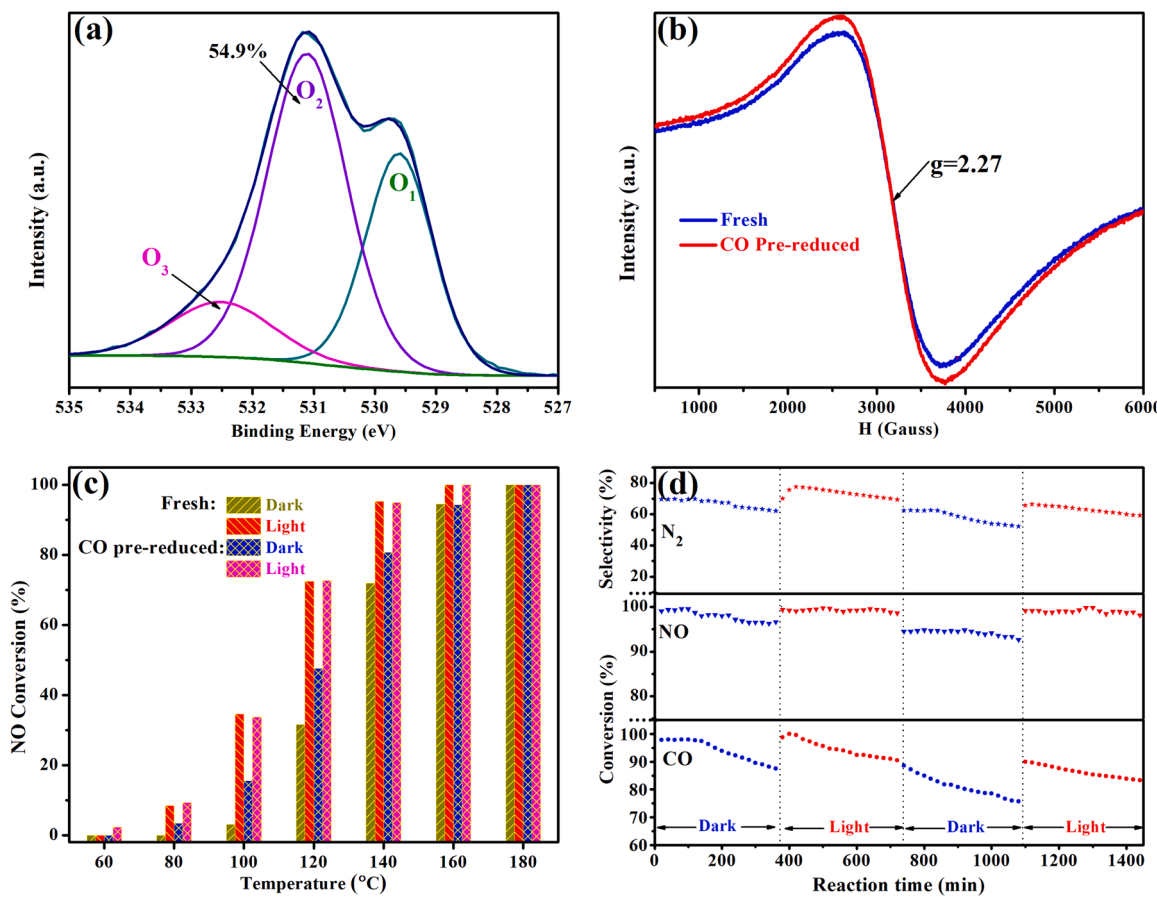


Fig. 6. (a) XPS spectra for the O1s level of CO pre-reduced NiCo₂O₄ sample. (b) EPR spectra of fresh and CO pre-reduced NiCo₂O₄ samples. (c) NO conversion over fresh and CO pre-reduced NiCo₂O₄ samples under visible light or in dark. (d) CO oxidation, NO conversion, and the selectivity of N₂ as function of reaction time over CO pre-reduced NiCo₂O₄ catalysts at 190 °C under visible light irradiation or in dark.

conversion while stable NO conversion meant that maybe preferential adsorption of NO on catalyst surface suppressed the adsorption and activation of CO. Herein, more NO would be reduced to N₂O (CO + 2NO → CO₂ + N₂O), and thus resulted in the decrease in N₂ selectivity. However, visible light illumination apparently suppressed the decaying trend (Fig. 6d). Moreover, the XRD pattern and FTIR results (Fig. S14 and S15) of NiCo₂O₄ after NO reduction by CO for 24 h testing showed a negligible change, which also well displayed the excellent stability of the catalyst itself.

In order to investigate the effect of H₂O on catalytic performance, a 5% H₂O was also added into the feed gas. The activity results over CO pre-reduced NiCo₂O₄ sample (Fig. S16) at low temperature showed an evident decrease in CO conversion, NO conversion and N₂ selectivity in the presence of 5% H₂O, which could be interpreted as the competitive adsorption between H₂O and CO/NO. Herein, the abundant H₂O would occupy the adsorption sites for CO and NO, while the deactivation effect could be well alleviated at higher temperatures (T > 150 °C) and visible light irradiation. Subsequently, we tested the impact of H₂O on catalytic stability at 220 °C. As presented in Fig. 7, the apparently declining NO conversion and N₂ selectivity could recover soon after removing H₂O, and visible light could further accelerate the process, which well demonstrated a good H₂O resistance and strong regeneration ability of as-prepared catalyst.

3.4. Insights into the photo-thermal catalytic NO reduction by CO mechanism

To better understand the connection between surface states of catalyst and catalytic activity, XPS testing of samples before and after

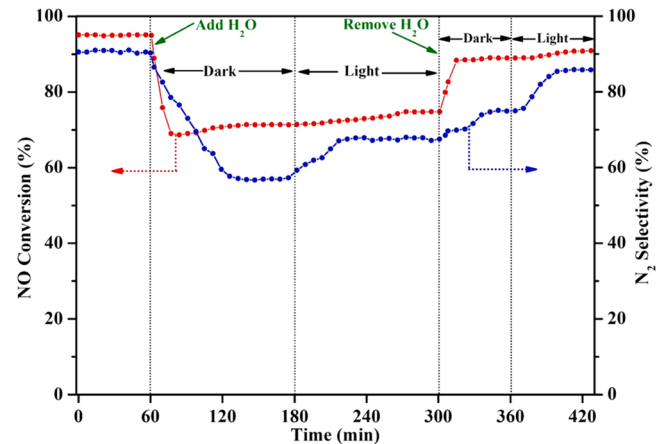


Fig. 7. Effect of H₂O on the NO conversion and N₂ selectivity as function of reaction time over CO pre-reduced NiCo₂O₄ at 220 °C under visible light or in dark.

the CO + NO reaction was performed. It has been well recognized that the lower binding energy (BE) value means the higher surface electron density. Combining the high-resolution O1s XPS spectra in Fig. 6a and Fig. 8a, we could see that the already increased VOs concentration in NiCo₂O₄ sample after CO + NO reaction in dark, which was mainly due to the dissociated NO or adsorptive nitrates and nitrites occupying the VOs, and then resulted in its decrease. However, the regenerated VOs

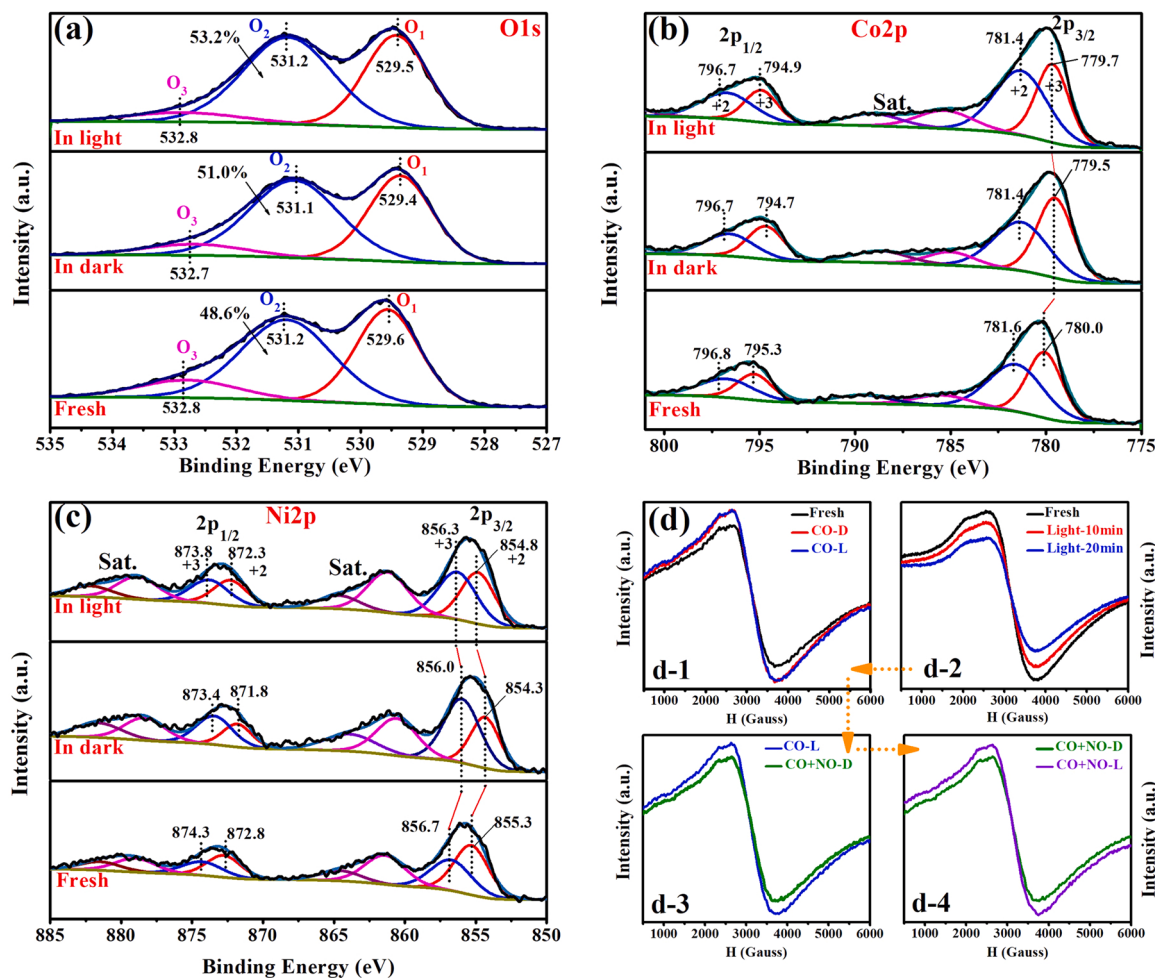


Fig. 8. High-resolution XPS spectra of (a) O1s, (b) Co2p, and (c) Ni2p over NiCo_2O_4 samples before and after $\text{CO} + \text{NO}$ reaction. (d) Quasi *in situ* EPR spectra of NiCo_2O_4 sample under different treatments: (Fresh) after N_2 pre-treatment for 2 h at 150°C , (In dark or D) after reacted at 150°C in dark, (In light or L) after reacted at 150°C under visible light irradiation.

(51.0% to 53.2%) after introducing visible light into the reaction process meant that the photo-excitation of NiCo_2O_4 could promote the migration out of the lattice oxygen and then form VOs. Herein, the catalyst surface lattice oxygen and chemical adsorption oxygen achieve a new equilibrium again, which driven the subsequent NO dissociation and reduction under a synergistic photo-thermal effect.

Fig. 8b and c presents the changes of Co2p and Ni2p over NiCo_2O_4 under different reaction conditions. Obviously, both the BE of Co2p and Ni2p after sample reacted in dark exhibited an obvious negative shift compared to the fresh and CO-reduced samples (Fig. S13), which could be attributed to the strong donor electron effect of CO as a reductive gas. However, the slight positive and restored BE values of Co2p and Ni2p after CO + NO reaction in light (still lower than that in fresh sample) also revealed an excellent stability and circulation of NiCo_2O_4 sample under a photo-thermal synergistic system. As compliment to XPS results, the quasi *in situ* EPR testing was also conducted to explore the VOs variation under different reaction conditions. Interestingly, as presented in Fig. 8d-2, visible light irradiating NiCo_2O_4 would resulted in an observably reduced VOs concentration (*i.e.* enhanced Co^{3+}) in the absence of CO or NO, which could be attributed an photocorrosion of sample itself under visible light illumination. Specifically, the more photo-induced hole of NiCo_2O_4 as a P-type semiconductor would bring about photooxidation of itself due to its narrow band gap. However, the already enhanced VOs amount after exposing NiCo_2O_4 sample into CO stream at 150°C would not decline when continuing to introduce visible light into above reaction process (Fig. 8d-1). The result convincingly

confirmed that CO would well trap the photo-induced hole and then was further promoted into CO_2 , which suppressed the photocorrosion of catalyst and simultaneously promoted the separation of its photo-generated carriers. As for $\text{CO} + \text{NO}$ reaction in dark (Fig. 8d-3), the obviously weaker EPR signal intensity compared to that for single CO indicated that NO would consume or fill the VOs induced by the foregoing CO. The continuous consumption of VOs also led to an unstable catalytic performance, while visible light irradiation would well recover the VOs again (Fig. 8d-4). This EPR variation tendency was also in line with above XPS results, fully embodied the positive effect of VOs on CO + NO reaction, consistent with the reports in previous works [7–9].

In order to comprehend the reaction mechanism of NO reduction by CO under photo-thermal synergistic effect in depth, the temperature-dependent *in situ* DRIFTS testing for CO, NO, and CO + NO adsorbed on NiCo_2O_4 sample was performed, respectively. Fig. 9 shows the DRIFTS spectra of CO interaction with catalyst sample with increasing temperature from room temperature to 220°C . As seen in it, two obvious twin IR bands observed at 2170 and 2110 cm^{-1} during the whole testing process were assigned to the P and R-branch of gaseous CO [9]. Moreover, the bands at 2334 and 2365 cm^{-1} attributed to the formation of CO_2 were also observed (seeing the inset of Fig. 9) [10]. With the temperature increasing, the decreasing CO bands accompanied by the rising CO_2 and weakly varied H_2O band (seeing the inset of Fig. 9) indicated that CO would directly react with lattice oxygen of catalyst sample instead of surface hydroxyl in the absence of NO, and then reduced the NiCo_2O_4 . The results were also consistent with the

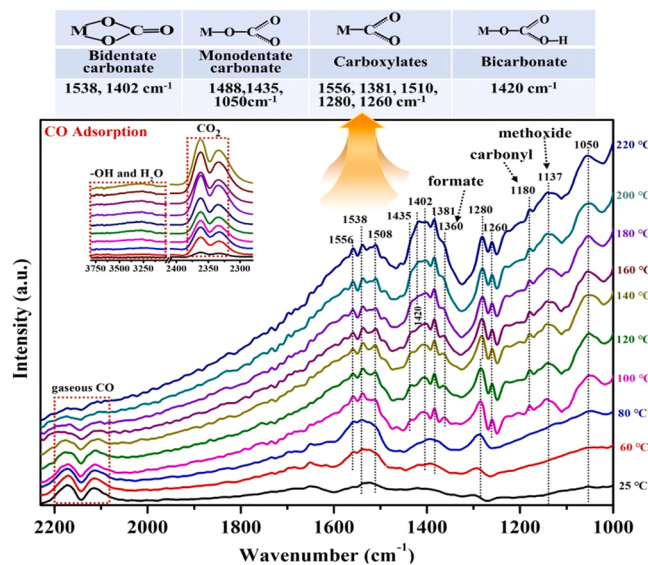


Fig. 9. *In situ* DRIFTS spectra of CO adsorbed on NiCo_2O_4 at different temperatures.

aforementioned catalytic activity and CO-TPR results. Specifically, the absorbed CO would fleetly convert into some intermediate species located from 1000 to 1700 cm^{-1} , especially when the temperature was above 80 °C. Herein, the bands at 1556 and 1381 cm^{-1} attributed to $\nu_s(\text{COO}^-)$ and $\nu_{as}(\text{COO}^-)$ vibration modes of carboxylates [9], and the bands around 1510, 1280, 1260 cm^{-1} also associated to carboxylate or carbonates species [10,27,30,57]. The peak at 1538 and 1402 cm^{-1} was ascribed to bidentate carbonates, while 1488, 1435, and 1050 cm^{-1} to monodentate carbonates, 1180 cm^{-1} to stretching vibration of carbonyl [7,10,27]. Additionally, the peak at 1360 cm^{-1} belonging to the bidentate formate [60] and 1137 cm^{-1} to the $\nu(\text{C}-\text{O})$ stretch of methoxide species [64] could be formed mainly because CO molecules interact with surface hydroxyls. As the increasing reaction temperature, the increased intensity of these bands suggested that CO molecules were continuously adsorbed and then converted into carbon-oxygen active species. Furthermore, the new band observed at 1420 cm^{-1} attributed to bicarbonate also implied that higher temperature was more favorite for the CO activation [57]. Note that the apparent upgrade baseline position with temperature going up could be explained that the continuous presence of excited electrons due to the formation of more high density state, which was associated with the existence of surface or sub-surface electron traps over catalyst sample [58]. As for CO adsorption under visible light irradiation at the identical condition (Fig. S17), no new peaks except the obvious decreased CO and increased CO_2 peaks were observed, which indicated that visible light illumination did not change the style of CO adsorption and activation.

With regard to the exposure of NiCo_2O_4 to NO at room temperature (Fig. 10), some IR bands appeared in the range of 900–2000 cm^{-1} , the bidentate nitrates at 1585, 1543, and 998 cm^{-1} [8,10,59], monodentate nitrates at 1497 and 1288 cm^{-1} [60], weak linear monodentate nitrite at 1442 cm^{-1} [13], hyponitrites at 1330 cm^{-1} [61], bridging nitrates at 1046 cm^{-1} [38]. The emergence of abundant IR bands mainly stemmed from NO interaction with lattice oxygen of catalyst surface, further indicating an excellent capacity of NiCo_2O_4 sample for NO adsorption and activation. Moreover, in the low temperature range of 60–80 °C, the increased H_2O band at 3300 cm^{-1} , CO_2 doublet peaks at 2361 and 2335 cm^{-1} , N_2O at 2239 cm^{-1} , -NCO species at 2207 cm^{-1} could be attributed to an interaction between NO and residual hydrocarbon (a negative band at 2950–3050 cm^{-1}) on catalyst surface. And the formation of isocyanate functional group (-NCO) could be regarded as a sensitive indicator for the NO dissociation [15,62]. These results well indicated that NiCo_2O_4 possessed an excellent ability for dissociating NO

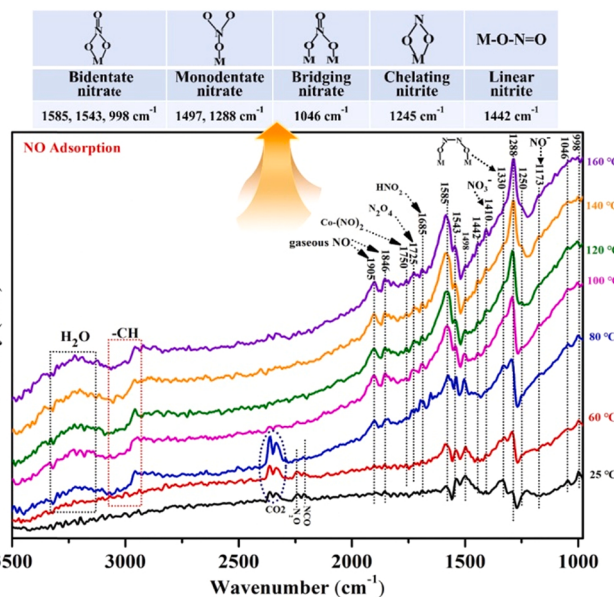


Fig. 10. *In situ* DRIFTS spectra of NO adsorbed on NiCo_2O_4 at different temperatures.

even at low temperature due to the presence of abundant VOs in it. Obviously, the intensity of all adsorption peaks enhanced with the increment of temperature ($> 80^\circ\text{C}$). Except for the peaks mentioned above, some new bands were also observed at 1758 cm^{-1} assigned to NO weakly adsorbed on $\text{Co}-(\text{NO})_2$ [10], 1725 cm^{-1} to N_2O_4 (obtained by adsorbed NO_2 dimerization) [63], 1685 cm^{-1} to cis- HNO_2 [59], 1410 cm^{-1} to ionic nitrates, 1245 cm^{-1} to chelating bidentate nitrite or nitrates and 1180 cm^{-1} to NO^- species [7,13,58,61]. The presence of gaseous NO peaks at 1905 and 1848 cm^{-1} at high temperature mainly resulted from the desorption of physical adsorbed NO [9,13]. The above results all suggested that elevating temperature could promote the NO adsorption and activation. Similar to CO adsorption on catalyst surface, the visible light irradiation also did not change the style of NO adsorption and activation (Fig. S18). Additionally, the apparent uplifted baseline position in the course of raising the temperature was also related to surface electron traps. However, note that the continuous NO adsorption would result in an accumulation of excessive nitrates intermediates on the catalyst surface, occupy the active sites, which was unbenefited to NO dissociation and reduction instead.

The *in situ* DRIFTS spectra of NO + CO interaction with NiCo_2O_4 catalysts in the simulated photo-thermal reaction conditions were also recorded. As depicted in Fig. 11, the obvious CO_2 bands (2361 and 2335 cm^{-1}), gaseous CO bands (2171 and 2113 cm^{-1}), and gaseous NO doublet peaks (1905 and 1851 cm^{-1}) were observed in this infrared spectra. In addition, several peaks were also detected in the region of 1800–1000 cm^{-1} upon co-adsorption CO and NO at room temperature, corresponding to different active species adsorbed on catalyst surface. Thereinto, the peaks at 1575 cm^{-1} were assigned to bidentate nitrates, 1530 cm^{-1} to bidentate carbonate, 1478 cm^{-1} to monodentate carbonate, 1444 and 1300 cm^{-1} to weak monodentate nitrate [13], 1063 cm^{-1} to bridging nitrates or monodentate carbonates. As compared to the case of NiCo_2O_4 adsorbing single CO or NO at 25 °C, both formed carbonates and nitrates were very weak in intensities. While two peaks at 2235 and 2207 cm^{-1} separately assigned to N_2O and -NCO species was more prominent upon the co-presence of CO and NO. Herein, the N_2O and -NCO as important intermediates could be regarded as the indicators of NO dissociation [15,62]. The above results well confirmed that NO was dissociated and reduced in the presence of reductive CO gas, and then generated CO_2 and N_2O in the low temperature, which also led to a decrease in adsorbed carbonate, carboxylate,

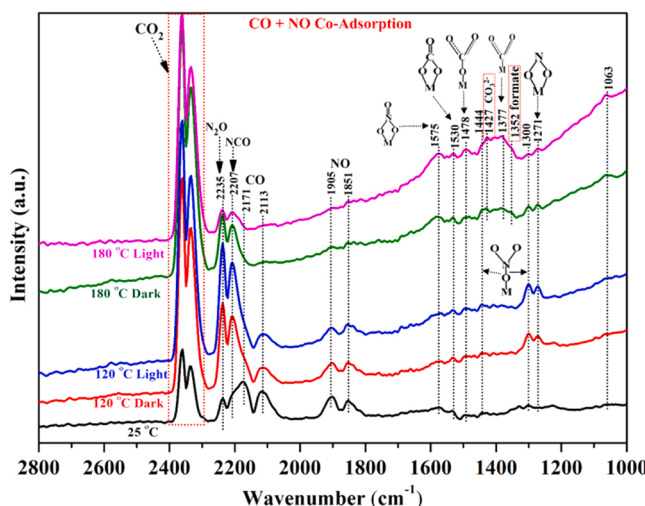


Fig. 11. *In situ* DRIFTS spectra of CO and NO co-adsorption on NiCo_2O_4 at different temperatures.

and nitrates peaks due to their fast conversion and consumption.

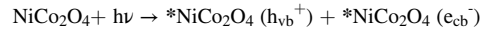
With increasing reaction temperature to 120°C (an obvious NO conversion at this point), the enhanced monodentate nitrate peak at 1300 cm^{-1} [13] and emerging peak attributed to monodentate nitrite or nitro species at 1271 cm^{-1} [38] indicated that elevating temperature was indeed favorite for the activation of NO. Whereas, their intensities including those mentioned IR peaks above were still much weaker than what they formed in the case of NO adsorption alone, which suggested that the surface reconstruction of catalyst induced by CO would effectively inhibited the NO oxidation to form excessive nitrates or accelerated their rapid transformation and reduction. This result also implied that the monodentate nitrate and nitrite might act as the major intermediate during the CO + NO reaction at current conditions. Simultaneously, the obvious shrinking CO gaseous peaks and increased N_2O , -NCO, and CO_2 also revealed that the decomposed NO_x or dissociated NO over VOs were mainly transformed and reduced into N_2O by-product instead of N_2 , and visible light irradiation further reinforced the process due to promoted more VOs formation. But even so, the selectivity of N_2 was still quite poor because the NO with unpaired electron was preferentially adsorbed on the surface of catalyst, concurrently inhibited the CO adsorption, and then inactivated the subsequent reduction process gradually.

As for increasing the reaction temperature to 180°C , the CO and NO peaks further decreased and were almost disappeared, while more CO_2 formation and apparently decreased N_2O and -NCO indicated higher temperature not only boosted NO reduction by CO, but also suppressed the N_2O production and thus increased the N_2 selectivity ($\text{CO} + \text{N}_2\text{O} = \text{CO}_2 + \text{N}_2$), which was well concord with the results of catalytic performance. Moreover, some new phenomena were also observed during the higher heating process. The monodentate nitrate (1300 cm^{-1}) and monodentate nitrite (1271 cm^{-1}) significantly decreased due to their poor thermal stability at higher reaction temperature. Instead, surface carbonate (1427 cm^{-1}), carboxylate (1377 cm^{-1}), and formate (1352 cm^{-1}) increased, which could be explained that the desorption or dissociation of adsorbed NO_x species at high temperature would expose active sites to adsorb and activate CO. In return, the adsorbed CO would capture more lattice oxygen to generate CO_2 and more VOs, and then drove NO dissociation. Moreover, compared with single NO adsorption on NiCo_2O_4 sample, the vibration bands of enhanced bidentate nitrate in the mixture atmosphere shifted to lower wavenumber at this temperature (from 1585 to 1575 cm^{-1}), which could be owing to d-electron transfer from the metal cation to the antibonding orbital of NO and then favorite for weakening the N-O bond. With the introduction of visible light at the identical condition, monodentate nitrate (1300 cm^{-1}) and

nitrite (1271 cm^{-1}) were almost disappeared, while -CO_x intermediates species further increased notably, which suggested that visible light irradiation was more favorite for CO activation by suppressing NO_x accumulation. Combining the above XPS and EPR results concurrently, it meant that more VOs induced by CO activation at higher temperature would further expedite the NO dissociation, also suppressed the NO_x generation in turn. The speculation was well supported by the continuously decreased N_2O and -NCO species under visible light illumination, also implied the enhancement of N_2 selectivity.

Based on the above results and discussions, a proposed mechanism of NO reduction by CO over metastable NiCo_2O_4 catalyst under a photo-thermal synergic effect was described as follows:

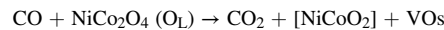
3.4.1. Photo-excitation of NiCo_2O_4



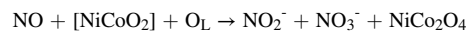
- Note that the more photo-generate hole of NiCo_2O_4 as a P-type semiconductor would bring about a photooxidation of itself due to its narrow band gap.

3.4.2. Adsorption and activation processes of CO and NO under the reaction temperature below 100°C

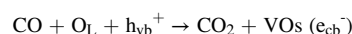
- Herein, CO would directly trap the surface lattice oxygen (O_L) of metastable NiCo_2O_4 to eventually generate CO_2 and VOs according to the Mars-van Krevelen mechanism, simultaneously resulted in a reduction of catalyst itself. Note that the $[\text{NiCoO}_2]$ was denoted as reductive NiCo_2O_4 sample.



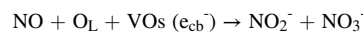
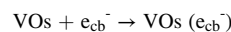
- The majority of NO adsorbed on catalyst surface were only transformed into nitrate and nitrite rather than dissociation, and then these products also filled up the VOs in turn.



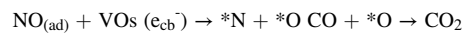
- The photo-induced hole (h_{vb}^+) further promoted the CO oxidation and production of more VOs, also concurrently promoted the separation of photo-induced charge carriers.



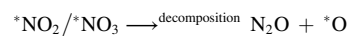
3.4.3. Promoted adsorption and activation processes of CO and NO under the reaction temperature over 100°C



- Pathway I: NO dissociation at electron-rich VOs, but not a main pathway.



- Pathway II: Adsorbed NO_x intermediates (nitrate and nitrite) decomposition, a main pathway.

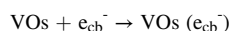
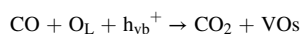
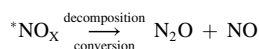




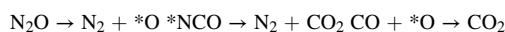
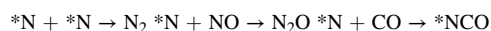
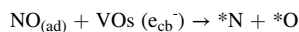
- Note that the decomposed NO_x was only reduced into N_2O instead of N_2 owing to a less dissociation energy of nitrate or nitrite to form N_2O and high activation energy of N_2O to N_2 .

3.4.4. Promoted adsorption and activation processes of CO and NO under the reaction temperature over 150°C

- The higher temperature would be beneficial to the desorption, dissociation and decomposition of NO_x species, which exposed active sites to adsorb and activate CO. The adsorbed CO would capture more lattice oxygen to generate CO_2 and more VOs in turn, and then driven the NO dissociation into N_2 .



- NO dissociation, a main pathway.



The above proposed mechanism of NO reduction by CO over metastable NiCo_2O_4 under a photo-thermal synergistic effect could be also described in Fig. 12. During the processes, the more VOs induced by CO played a key role in NO reduction, and visible light irradiation further facilitated this step by enhancing the ability of CO capturing lattice oxygen and VOs enriching electrons. The increasing in reaction temperature would accelerated the gradually transformation of NO to N_2O , and then finally into N_2 .

4. Conclusion

In this work, the metastable NiCo_2O_4 sample was fabricated by a two-step solvothermal-calcination method. After evaluating its catalytic performance for NO reduction by CO under photo-thermal synergistic effect and combining with the above characterization and results, the following conclusions could be drawn:

- Compared to NCO-450 and NCO-650, metastable NCO-250 annealed at lower temperature exhibited better catalytic activity and higher N_2 selectivity for $\text{CO} + \text{NO}$ reaction due to its stronger transfer ability of surface lattice oxygen and the existence of more VOs in it.
- At low temperature, CO would react with surface lattice oxygen of catalyst to generate VOs, and then induce a surface reconstruction of NiCo_2O_4 sample. With the increase in reaction temperature, the formed VOs drove the successively transformation of NO into NO_x , N_2O , and then finally N_2 .
- Visible light irradiation would further promote CO oxidation into CO_2 by enhancing its ability to capture lattice oxygen, and thus generate more VOs in NiCo_2O_4 . The process of photo-generated hole trapped by CO would also in turn expedite the separation of charge carriers, and then electrons-rich VOs boosted NO adsorption and activation. This work shows that the synergistic effect of metastable property and photo-excitation behavior of catalyst sample could assist the thermocatalytic NO reduction by inducing more VOs generation.

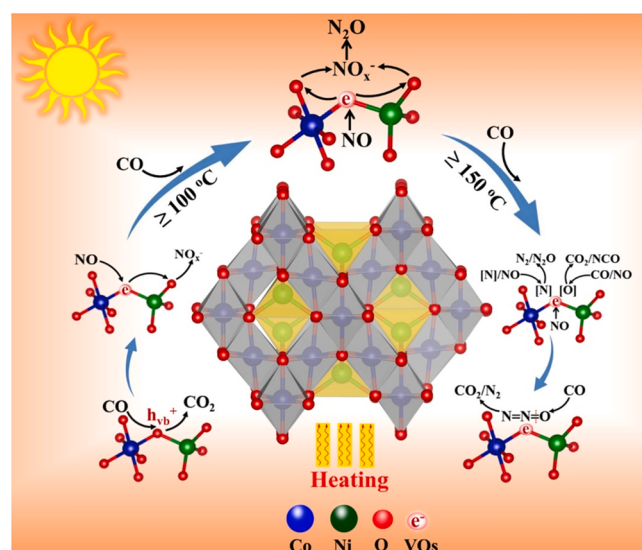


Fig. 12. The proposed photo-thermal catalytic process of NO reduction by CO over NiCo_2O_4 .

CRediT authorship contribution statement

Gang Cheng: Conceptualization, Investigation, Formal analysis, Writing – review & editing. **Xinjie Song:** Investigation. **Xun Chen:** Resources, Data curation. **Wenxin Dai:** Conceptualization, Funding acquisition, Formal analysis, Writing – review & editing.

Declaration of Competing Interest

The authors declare that they have no known competing financial interests or personal relationships that could have appeared to influence the work reported in this paper.

Acknowledgments

This work was financially supported by the National Natural Science Foundation of China (no. 21872030) and Key Program of Qingyuan Innovation Laboratory (Grant No. 00121001).

Appendix A. Supporting information

Supplementary data associated with this article can be found in the online version at doi:10.1016/j.apcatb.2021.120988.

References

- [1] Q. Wu, R. van de Krol, Selective photoreduction of nitric oxide to nitrogen by nanostructured TiO_2 photocatalysts: role of oxygen vacancies and iron dopant, *J. Am. Chem. Soc.* 134 (2012) 9369–9375.
- [2] F. Xing, J. Jeon, T. Toyao, K.I. Shimizu, S. Furukawa, A Cu-Pd single-atom alloy catalyst for highly efficient NO reduction, *Chem. Sci.* 10 (2019) 8292–8298.
- [3] L. Savereide, S.L. Nauert, C.A. Roberts, J.M. Notestein, The effect of support morphology on $\text{CoO}_x/\text{CeO}_2$ catalysts for the reduction of NO by CO, *J. Catal.* 366 (2018) 150–158.
- [4] H.-o Zhu, J.-R. Kim, S.-K. Ihm, Characteristics of $\text{Pt}/\text{WO}_3/\text{CeO}_2/\text{ZrO}_2$ catalysts for catalytic reduction of NO by CO, *Appl. Catal. B: Environ.* 86 (2009) 87–92.
- [5] M. Li, X. Wu, Y. Cao, S. Liu, D. Weng, R. Ran, NO reduction by CO over Rh/ Al_2O_3 and Rh/ AlPO_4 catalysts: Metal-support interaction and thermal aging, *J. Colloid Interface Sci.* 408 (2013) 157–163.
- [6] K. Huang, L. Lin, K. Yang, W. Dai, X. Chen, X. Fu, Promotion effect of ultraviolet light on NO + CO reaction over Pt/TiO₂ and Pt/CeO₂-TiO₂ catalysts, *Appl. Catal. B: Environ.* 179 (2015) 395–406.
- [7] G. Cheng, X. Tan, X. Song, X. Chen, W. Dai, R. Yuan, X. Fu, Visible light assisted thermocatalytic reaction of CO + NO over Pd/LaFeO₃, *Appl. Catal. B: Environ.* 251 (2019) 130–142.

- [8] X. Tan, G. Cheng, X. Song, X. Chen, W. Dai, X. Fu, The promoting effect of visible light on the CO + NO reaction over the Pd/N-TiO₂ catalyst, *Catal. Sci. Technol.* 9 (2019) 3637–3646.
- [9] X. Yao, Y. Xiong, W. Zou, L. Zhang, S. Wu, X. Dong, F. Gao, Y. Deng, C. Tang, Z. Chen, L. Dong, Y. Chen, Correlation between the physicochemical properties and catalytic performances of Ce_xSn_{1-x}O₂ mixed oxides for NO reduction by CO, *Appl. Catal. B: Environ.* 144 (2014) 152–165.
- [10] L. Wang, X. Cheng, Z. Wang, C. Ma, Y. Qin, Investigation on Fe-Co binary metal oxides supported on activated semi-coke for NO reduction by CO, *Appl. Catal. B: Environ.* 201 (2017) 636–651.
- [11] X. Zhang, X. Cheng, C. Ma, Z. Wang, Effects of the Fe/Ce ratio on the activity of CuO/CeO₂–Fe₂O₃ catalysts for NO reduction by CO, *Catal. Sci. Technol.* 8 (2018) 3336–3345.
- [12] X. Shi, B. Chu, F. Wang, X. Wei, L. Teng, M. Fan, B. Li, L. Dong, L. Dong, Mn-modified CuO, CuFe₂O₄, and gamma-Fe₂O₃ three-phase strong synergistic coexistence catalyst system for NO reduction by CO with a wider active window, *ACS Appl. Mater. Interfaces* 10 (2018) 40509–40522.
- [13] H. Liu, L. Liu, L. Wei, B. Chu, Z. Qin, G. Jin, Z. Tong, L. Dong, B. Li, Preparation of three-dimensionally ordered macroporous MFe₂O₄ (M = Co, Ni, Cu) spinel catalyst and its simultaneous catalytic application in CO oxidation and NO + CO reaction, *Fuel* 272 (2020).
- [14] Y. Wang, A. Zhu, Y. Zhang, C.T. Au, X. Yang, C. Shi, Catalytic reduction of NO by CO over NiO/CeO₂ catalyst in stoichiometric NO/CO and NO/CO/O₂ reaction, *Appl. Catal. B: Environ.* 81 (2008) 141–149.
- [15] Y. Lv, L. Liu, H. Zhang, X. Yao, F. Gao, K. Yao, L. Dong, Y. Chen, Investigation of surface synergistic oxygen vacancy in CuO-CoO binary metal oxides supported on gamma-Al₂O₃ for NO removal by CO, *J. Colloid Interface Sci.* 390 (2013) 158–169.
- [16] S. Roy, M.S. Hegde, G. Madras, Catalysis for NO_x abatement, *Appl. Energy* 86 (2009) 2283–2297.
- [17] T.C. Peck, G.K. Reddy, C.A. Roberts, Monolayer supported CuO_x/Co₃O₄ as an active and selective low temperature NO_x decomposition catalyst, *Catal. Sci. Technol.* 9 (2019) 1132–1140.
- [18] G.M.L. Simonot, A comparative study of LaCoO₃, Co₃O₄ and a mix of LaCoO₃–Co₃O₄: II. Catalytic properties for the CO + NO reaction, *Appl. Catal. B: Environ.* 11 (1997) 181–191.
- [19] H. Hu, S. Cai, H. Li, L. Huang, L. Shi, D. Zhang, In Situ DRIFTS investigation of the low-temperature reaction mechanism over Mn-doped Co₃O₄ for the selective catalytic reduction of NO_x with NH₃, *J. Phys. Chem. C* 119 (2015) 22924–22933.
- [20] K. Tang, W. Liu, J. Li, J. Guo, J. Zhang, S. Wang, S. Niu, Y. Yang, The effect of exposed facets of ceria to the nickel species in nickel-ceria catalysts and their performance in a NO + CO reaction, *ACS Appl. Mater. Interfaces* 7 (2015) 26839–26849.
- [21] J. Liu, X. Li, R. Li, Q. Zhao, J. Ke, H. Xiao, L. Wang, S. Liu, M. Tadé, S. Wang, Facile synthesis of tube-shaped Mn-Ni-Ti solid solution and preferable Langmuir–Hinshelwood mechanism for selective catalytic reduction of NO by NH₃, *Appl. Catal. A: Gen.* 549 (2018) 289–301.
- [22] Y. Gou, X. Liang, B. Chen, Porous Ni–Co bimetal oxides nanosheets and catalytic properties for CO oxidation, *J. Alloy. Compd.* 574 (2013) 181–187.
- [23] X. Wang, W. Wen, J. Mi, X. Li, R. Wang, The ordered mesoporous transition metal oxides for selective catalytic reduction of NO_x at low temperature, *Appl. Catal. B: Environ.* 176–177 (2015) 454–463.
- [24] Y. Liu, J. Xu, H. Li, S. Cai, H. Hu, C. Fang, L. Shi, D. Zhang, Rational design and in situ fabrication of MnO₂@NiCo₂O₄ nanowire arrays on Ni foam as high-performance monolith-NO_x catalysts, *J. Mater. Chem. A* 3 (2015) 11543–11553.
- [25] Y. Duan, S. Sun, Y. Sun, S. Xi, X. Chi, Q. Zhang, X. Ren, J. Wang, S.J.H. Ong, Y. Du, L. Gu, A. Grimaud, Z.J. Xu, Mastering surface reconstruction of metastable spinel oxides for better water oxidation, *Adv. Mater.* 31 (2019), e1807898.
- [26] Z. Li, J. Liu, Y. Zhao, R. Shi, G.I.N. Waterhouse, Y. Wang, L.-Z. Wu, C.-H. Tung, T. Zhang, Photothermal hydrocarbon synthesis using alumina-supported cobalt metal nanoparticle catalysts derived from layered-double-hydroxide nanosheets, *Nano Energy* 60 (2019) 467–475.
- [27] M. Xu, S. Yao, D. Rao, Y. Niu, N. Liu, M. Peng, P. Zhai, Y. Man, L. Zheng, B. Wang, B. Zhang, D. Ma, M. Wei, Insights into interfacial synergistic catalysis over Ni@TiO_{2-x} catalyst toward water-gas shift reaction, *J. Am. Chem. Soc.* 140 (2018) 11241–11251.
- [28] X. Lin, L. Lin, K. Huang, X. Chen, W. Dai, X. Fu, CO methanation promoted by UV irradiation over Ni/TiO₂, *Appl. Catal. B: Environ.* 168–169 (2015) 416–422.
- [29] Z. Ren, V. Botu, S. Wang, Y. Meng, W. Song, Y. Guo, R. Ramprasad, S.L. Suib, P. X. Gao, Monolithically integrated spinel M_xCo_{3-x}O₄ (M=Co, Ni, Zn) nanoarray catalysts: scalable synthesis and cation manipulation for tunable low-temperature CH₄ and CO oxidation, *Angew. Chem. Int. Ed.* 53 (2014) 7223–7227.
- [30] Y. Yi, P. Zhang, Z. Qin, C. Yu, W. Li, Q. Qin, B. Li, M. Fan, X. Liang, L. Dong, Low temperature CO oxidation catalysed by flower-like Ni–Co–O: how physicochemical properties influence catalytic performance, *RSC Adv.* 8 (2018) 7110–7122.
- [31] S. Wang, B.Y. Guan, X.W. Lou, Rationally designed hierarchical N-doped carbon@NiCo₂O₄ double-shelled nanoboxes for enhanced visible light CO₂ reduction, *Energy Environ. Sci.* 11 (2018) 306–310.
- [32] D. Ouyang, J. Xiao, F. Ye, Z. Huang, H. Zhang, L. Zhu, J. Cheng, W.C.H. Choy, Strategic synthesis of ultrasmall NiCo₂O₄ NPs as hole transport layer for highly efficient perovskite solar cells, *Adv. Energy Mater.* 8 (2018).
- [33] C. Feng, Q. Zhou, B. Zheng, X. Cheng, Y. Zhang, Y. Bi, Ultrathin NiCo₂O₄ nanosheets with dual-metal active sites for enhanced solar water splitting of a BiVO₄ photoanode, *J. Mater. Chem. A* 7 (2019) 22274–22278.
- [34] B. Han, J. Song, S. Liang, W. Chen, H. Deng, X. Ou, Y.-J. Xu, Z. Lin, Hierarchical NiCo₂O₄ hollow nanocages for photoreduction of diluted CO₂: adsorption and active sites engineering, *Appl. Catal. B: Environ.* 260 (2020).
- [35] S. Liu, L. Hu, X. Xu, A.A. Al-Ghamdi, X. Fang, Nickel cobaltite nanostructures for photoelectric and catalytic applications, *Small* 11 (2015) 4267–4283.
- [36] S. Wang, X. Hai, X. Ding, K. Chang, Y. Xiang, X. Meng, Z. Yang, H. Chen, J. Ye, Light-switchable oxygen vacancies in ultrafine Bi₅O₇Br nanotubes for boosting solar-driven nitrogen fixation in pure water, *Adv. Mater.* 29 (2017).
- [37] T. Hou, Y. Xiao, P. Cui, Y. Huang, X. Tan, X. Zheng, Y. Zou, C. Liu, W. Zhu, S. Liang, L. Wang, Operando oxygen vacancies for enhanced activity and stability toward nitrogen photofixation, *Adv. Energy Mater.* 9 (2019).
- [38] G. Cheng, X. Liu, X. Song, X. Chen, W. Dai, R. Yuan, X. Fu, Visible-light-driven deep oxidation of NO over Fe doped TiO₂ catalyst: Synergic effect of Fe and oxygen vacancies, *Appl. Catal. B: Environ.* 277 (2020).
- [39] X. Song, G. Qin, G. Cheng, W. Jiang, X. Chen, W. Dai, X. Fu, Oxygen defect-induced NO[·] intermediates promoting NO deep oxidation over Ce doped SnO₂ under visible light, *Appl. Catal. B: Environ.* 284 (2021).
- [40] M. Kuang, J. Zhang, D. Liu, H. Tan, K.N. Dinh, L. Yang, H. Ren, W. Huang, W. Fang, J. Yao, X. Hao, J. Xu, C. Liu, L. Song, B. Liu, Q. Yan, Amorphous/crystalline heterostructured cobalt–vanadium–iron(oxy)hydroxides for highly efficient oxygen evolution reaction, *Adv. Energy Mater.* 10 (2020).
- [41] X. Li, L. Xiao, L. Zhou, Q. Xu, J. Wang, J. Xu, B. Liu, Adaptive bifunctional electrocatalyst of amorphous CoFe Oxide @ 2D black phosphorus for overall water splitting, *Angew. Chem. Int. Ed.* 59 (2020) 21106–21113.
- [42] J. Hu, S. Li, Y. Li, J. Wang, Y. Du, Z. Li, X. Han, J. Sun, P. Xu, A crystalline–amorphous Ni–Ni(OH)₂ core–shell catalyst for the alkaline hydrogen evolution reaction, *J. Mater. Chem. A* 8 (2020) 23232–23239.
- [43] B. Wang, M. Wang, L. Han, Y. Hou, W. Bao, C. Zhang, G. Feng, L. Chang, Z. Huang, J. Wang, Improved activity and SO₂ resistance by Sm-modulated redox of MnCeSmTiO_x mesoporous amorphous oxides for low-temperature NH₃-SCR of NO, *ACS Catal.* 10 (2020) 9034–9045.
- [44] L. Zhang, R. Tong, S.E. Shirasath, Y. Yang, G. Dong, The crystalline/amorphous stacking structure of SnO₂ microspheres for excellent NO photocatalytic performance, *J. Mater. Chem. A* (2021).
- [45] D. Liu, C. Zhang, Y. Yu, Y. Shi, Y. Yu, Z. Niu, B. Zhang, Hydrogen evolution activity enhancement by tuning the oxygen vacancies in self-supported mesoporous spinel oxide nanowire arrays, *Nano Res.* 11 (2017) 603–613.
- [46] D. Luo, G. Li, Y.P. Deng, Z. Zhang, J. Li, R. Liang, M. Li, Y. Jiang, W. Zhang, Y. Liu, W. Lei, A. Yu, Z. Chen, Synergistic engineering of defects and architecture in binary metal chalcogenide toward fast and reliable lithium–sulfur batteries, *Adv. Energy Mater.* 9 (2019).
- [47] Y. Zeng, Z. Lai, Y. Han, H. Zhang, S. Xie, X. Lu, Oxygen-vacancy and surface modulation of ultrathin nickel cobaltite nanosheets as a high-energy cathode for advanced Zn-ion batteries, *Adv. Mater.* (2018), 1802396.
- [48] B. Wei, J. Wu, G. Mei, Z. Qi, W. Hu, Z. Wang, NiCo₂O₄ nanowire arrays rich in oxygen deficiencies for hydrogen evolution reaction, *Int. J. Hydrogen Energy* 44 (2019) 6612–6617.
- [49] L. Ma, X. Shen, Z. Ji, X. Cai, G. Zhu, K. Chen, Porous NiCo₂O₄ nanosheets/reduced graphene oxide composite: facile synthesis and excellent capacitive performance for supercapacitors, *J. Colloid Interface Sci.* 440 (2015) 211–218.
- [50] Z. Qiu, Y. Ma, T. Edvinsson, In operando Raman investigation of Fe doping influence on catalytic NiO intermediates for enhanced overall water splitting, *Nano Energy* 66 (2019).
- [51] A.J.E. Rettie, K.C. Klavetter, J.-F. Lin, A. Dolocan, H. Celio, A. Ishiekwene, H. L. Bolton, K.N. Pearson, N.T. Hahn, C.B. Mullins, Improved visible light harvesting of WO₃ by incorporation of sulfur or iodine: a tale of two impurities, *Chem. Mater.* 26 (2014) 1670–1677.
- [52] Q. Ren, S. Mo, R. Peng, Z. Feng, M. Zhang, L. Chen, M. Fu, J. Wu, D. Ye, Controllable synthesis of 3D hierarchical Co₃O₄ nanocatalysts with various morphologies for the catalytic oxidation of toluene, *J. Mater. Chem. A* 6 (2018) 498–509.
- [53] H. Wang, D. Yong, S. Chen, S. Jiang, X. Zhang, W. Shao, Q. Zhang, W. Yan, B. Pan, Y. Xie, Oxygen-vacancy-mediated exciton dissociation in BiOBr for boosting charge-carrier-involved molecular oxygen activation, *J. Am. Chem. Soc.* 140 (2018) 1760–1766.
- [54] N. Yang, H. Cheng, X. Liu, Q. Yun, Y. Chen, B. Li, B. Chen, Z. Zhang, X. Chen, Q. Lu, J. Huang, Y. Huang, Y. Zong, Y. Yang, L. Gu, H. Zhang, Amorphous/crystalline hetero-phase Pd nanosheets: one-pot synthesis and highly selective hydrogenation reaction, *Adv. Mater.* 30 (2018), 1803234.
- [55] X. Li, X. Yan, X. Lu, S. Zuo, Z. Li, C. Yao, C. Ni, Photo-assisted selective catalytic reduction of NO by Z-scheme natural clay based photocatalyst: insight into the effect of graphene coupling, *J. Catal.* 357 (2018) 59–68.
- [56] Q. Jing, H. Li, Hierarchical nickel cobalt oxide spinel microspheres catalyze mineralization of humic substances during wet air oxidation at atmospheric pressure, *Appl. Catal. B: Environ.* 256 (2019).
- [57] H. Yu, J. Li, Y. Zhang, S. Yang, K. Han, F. Dong, T. Ma, H. Huang, Three-in-one oxygen vacancies: whole visible-spectrum absorption, efficient charge separation, and surface site activation for robust CO₂ photoreduction, *Angew. Chem. Int. Ed.* 58 (2019) 3880–3884.
- [58] J. Araña, D. Garzón Sousa, O. González Díaz, E. Pulido Melián, J.M. Doña Rodríguez, Effect of NO₂ and NO₃[–]/HNO₃ adsorption on NO photocatalytic conversion, *Appl. Catal. B: Environ.* 244 (2019) 660–670.
- [59] M. Kantcheva, Cobalt supported on zirconia and sulfated zirconia I. FT-IR spectroscopic characterization of the NO_x species formed upon NO adsorption and NO_x/O₂ coadsorption, *J. Catal.* 223 (2004) 352–363.
- [60] X. Hou, J. Qian, L. Li, F. Wang, B. Li, F. He, M. Fan, Z. Tong, L. Dong, Preparation and investigation of iron–cerium oxide compounds for NO_x reduction, *Ind. Eng. Chem. Res.* 57 (2018) 16675–16683.

- [61] M. Mihaylov, K. Chakarova, K. Hadjiivanov, Formation of carbonyl and nitrosyl complexes on titania- and zirconia-supported nickel: FTIR spectroscopy study, *J. Catal.* 228 (2004) 273–281.
- [62] E. Ozensoy, D. Wayne, Goodman, Vibrational spectroscopic studies on CO adsorption, NO adsorption CO + NO reaction on Pd model catalysts, *Phys. Chem. Chem. Phys.* 6 (2004).
- [63] M. Yuan, W. Deng, S. Dong, Q. Li, B. Zhao, Y. Su, Montmorillonite based porous clay heterostructures modified with Fe as catalysts for selective catalytic reduction of NO with propylene, *Chem. Eng. J.* 353 (2018) 839–848.
- [64] Jeffrey R.S. Brownson, M. Isabel Tejedor-Tejedor, Anderson Anderson, Photoreactive Anatase Consolidation Characterized by FTIR Spectroscopy, *Chem. Mater.* 17 (2005) 6304–6310, <https://doi.org/10.1021/cm051568f>.